Phase-engineered 3D-printed metalenses for spatial and spectral control of underwater acoustic vortex beams

Chadi Ellouzi[1,†], Farhood Aghdasi[1], Ali Zabihi[1], Shuaiguo Zhao[2], Chen Shen ⬤[1,‡]

1 Department of Mechanical Engineering, Rowan University, Glassboro, New Jersey 08028, USA
2 Thomas Lord Department of Mechanical Engineering and Materials Science,
  Duke University, Durham, North Carolina 27708, USA
 Corresponding authors. E-mail: †chadie17@rowan.edu, ‡shenc@rowan.edu
  Received August 12, 2025; accepted December 11, 2025

ABSTRACT

Acoustic vortex beams, which inherently carry orbital angular momentum, are emerging as powerful tools for applications ranging from particle manipulation to biomedical imaging and underwater communication. However, generating such beams with precise spatial control remains challenging and often requires complex transducer arrays. In this study, we introduce a unified design framework for tailoring underwater acoustic vortex beams using 3D-printed metalenses. By engineering the local phase profile of the metalens, this approach enables distinct functionalities, including the generation of tilted vortex beams, precise control of off-axis singularities, and the creation of dual-focus vortex beams via coaxial spiral zones. Furthermore, a frequency multiplexing strategy is implemented in the dual-focus configuration, enabling independent control of vortex foci at distinct frequencies using a single compact lens. The ability of these metalenses to shape acoustic pressure fields with high precision is validated through both numerical simulations and underwater measurements. This work demonstrates a versatile, fabrication-ready platform for the tunable spatial and spectral control of acoustic vortex beams, offering new possibilities for applications in acoustofluidics, therapeutic ultrasound, and underwater sensing and communication.

Keywords metamaterials, acoustic vortex, ultrasound
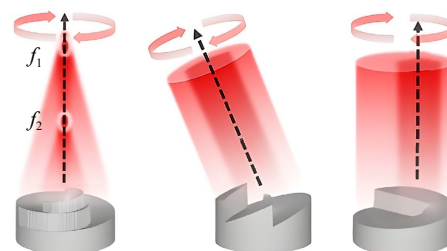
1 Introduction

Acoustic vortex beams are a class of waves with a unique wavefront distribution that carries orbital angular momentum, a property characterized by a spiraling phase and a central pressure null [1–3]. These beams exhibit unique capabilities for manipulating matter, encoding information, and concentrating acoustic energy in spatially structured ways. These properties make them valuable in applications ranging from contactless particle manipulation and acoustofluidic transport to noninvasive medical therapies and underwater communications [4–10]. To harness the unique properties of acoustic vortices, various strategies have been developed to generate beams with well-defined orbital angular momentum [11–13]. Liu *et al.* [14] introduced a metasurface of four gradient meta-atoms with a $\pi/2$ phase difference, enabling broadband vortex beam generation from 2.56 to 2.96 kHz. Similarly, an acoustic tweezer with

intertwined spiral electrodes operating at 43.5 MHz was designed to trap and position individual cells [15]. Other approaches include an ultrathin metasurface of polymer fibers and beads made via paper-cutting, which achieves high transmittance vortices from 5 to 30 kHz [16]. Additionally, azimuthally varying thickness structures fabricated with 3D-printed lenses have been used to generate single and double vortices at 1 MHz [17].

Furthermore, other studies have focused on manipulating vortex beams through single or dual-focus setups with shared or differing topological charges [18–21]. For instance, a single transducer combined with a PDMS lens embedding a helical phase structure generated focused acoustic vortices at 500 kHz for particle trapping and positioning of individual cells [22]. Jiménez-Gambín et al. [23] used phase-conjugated acoustic holograms and a spherically focused transducer at 500 kHz to produce vortices capable of penetrating the human skull, promising for biomedical applications and tumor control. Additionally, an optimized 3D-printed four-step Fresnel lens was introduced to generate efficient acoustic vortices using a 1 MHz transducer [24], while Li et al. [25] developed a chirality-tunable vortex tweezing device using coaxial ring transducers at 1 and 3.3 MHz with a holographic chiral lens. Moreover, advanced control over vortex orientation and trajectory has been explored through numerical studies on acoustic singularities in stratified media, revealing bending, stretching, migration, and angular momentum variations [26]. For example, an acoustic orbital Hall effect model was proposed showing transverse vortex shifts in inhomogeneous media, resulting in angled vortices [27]. Spatial control has further improved with off-axis vortex generation, where phase singularities shift laterally without changing beam direction. Ding et al. [28] achieved multitarget manipulation via phase-controlled sector-vortex transducer arrays at 1 MHz. Subsequent works introduced superimposition algorithms for multiple off-axis vortices using phase-coded circular arrays [29], and arrays generating fields with multiple off-axis vortices combining quasi-plane and coaxial non-vortex beams have been developed [30]. Recent advances in topological acoustics have further enriched the manipulation of acoustic vortex beams by leveraging chirality and nonreciprocity for robust information transport and directional control. For instance, chirality-protected designs have enabled extreme asymmetric acoustic information transport with inherent noise immunity, ensuring stable vortex propagation even in turbulent environments [31]. Complementing this, the rotational Doppler effect has been harnessed to achieve topological beam nonreciprocity, allowing precise breaking of time-reversal symmetry for unidirectional vortex steering [32].

Although significant research has explored acoustic vortices and their diverse applications, several challenges remain in achieving effective manipulation and integrating multiple vortices within a compact, versatile device. These challenges include the reliance on complex transducer array architectures [33–35], intricate phase field and complex metasurface designs [36–39], and constraints in achieving multifunctional operations with spatial control of the vortex beams. These limitations can lead to unwanted effects like acoustic wave reflection and refraction, ultimately distorting the shape and directionality of the acoustic beam [40]. As such, many functionalities that are well-established in optical vortex systems such as dynamic vortex redirection have yet to be fully developed or experimentally realized in their acoustic counterparts [41, 42]. These gaps motivate the development of simpler and more versatile approaches for spatially and spectrally controlled acoustic vortex beams.

In this study, a versatile and unified design framework for the generation and control of acoustic vortex beams using 3D-printed spiral phase metalenses is presented. By precisely engineering the local phase distribution, we demonstrate a range of advanced wavefront functionalities, including the formation of tilted vortex beams via forked phase encoding, the controlled placement of off-axis singularities, and the creation of dual-focus vortex beams through coaxial spiral zone configurations. Notably, for the dual-focus configuration, we introduce a frequency multiplexing strategy that enables independent control of multiple vortex foci at distinct operating frequencies through the use of a single lens and source. The performance of each proposed lens is validated through both numerical simulations and underwater experimental measurements, revealing highly controllable acoustic pressure fields with tunable spatial and spectral properties. This work establishes a low-complexity, fabrication-ready platform for multifunctional acoustic vortex manipulation and paves the way for compact, adaptive acoustic systems in applications such as targeted ultrasound therapy, acoustofluidic manipulation, and multi-channel underwater communication.

2 Numerical analysis

2.1 Concept and design of phase-engineered metalenses

The generation and control of acoustic vortex beams rely on imparting a helical phase distribution along their propagation path, which can be achieved using spiral phase metalenses. These metalenses are designed to impose an azimuthally varying phase delay across the aperture by modulating their local geometry, typically achieved through thickness variation to shape a vortex-like outgoing acoustic field. By carefully designing the phase profile, it becomes possible to tailor the properties of the resulting vortex beam. This enables functionalities such as splitting the beam into multiple vortices, steering its axis, or displacing its core. In this work, we propose a

085201-2

Chadi Ellouzi, et al., Front. Phys. 21(8), 085201 (2026)
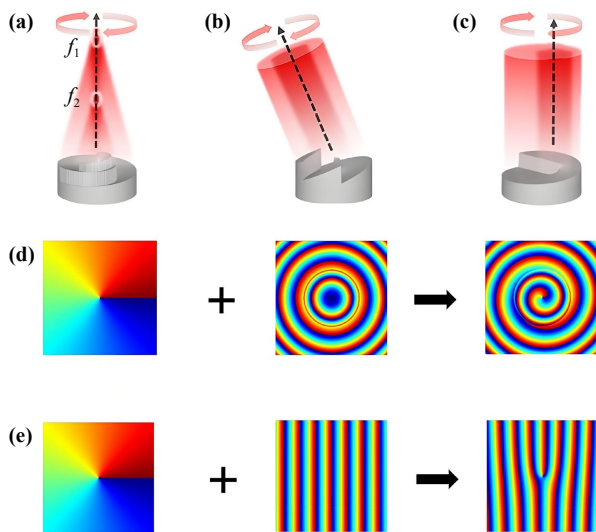
Fig. 1 Schematic of the proposed spiral phase metalenses and their concept. **(a)** Spiral metalens for double-focused acoustic vortex beam generation. **(b)** Spiral metalens for tilted vortex beam generation. **(c)** Spiral metalens for off-axis vortex beam generation. **(d)** The calculated phase distribution of a spiral phase, a focused lens phase, and their integration for $l = 1$ for the case of spiral metalens for double focused acoustic vortex beam generation. **(e)** The calculated phase distribution of a spiral phase, a blazed phase, and their integration for $l = 1$ for the case of spiral metalens for tilted vortex beam generation.

unified design framework that allows the design of various spiral phase metalenses with distinct functionalities, namely a double-focused acoustic vortex with different foci at different frequencies, a tilted vortex beam, and an off-axis vortex beam. These functionalities are illustrated schematically in Fig. 1, providing an overview of the metalens configurations and the resulting beam patterns. The general principle of operation is based on spatial phase design, which is realized by implementing a smooth thickness variation of the metalens facilitated by 3D printing. Each functionality requires distinct mathematical formulations and design strategies, which will be discussed in the following subsections.

2.1.1 Double focused acoustic vortex beam generation

To achieve the simultaneous or separate generation of two focused acoustic vortex beams at distinct frequencies and spatial locations, a frequency-multiplexed metalens design is employed. This configuration is based on a concentric dual-ring structure, where the inner ring is engineered to generate a vortex beam at frequency f_1 and focal point F_1, and the outer ring is designed to produce a second vortex at frequency f_2 with a focal point F_2. Each ring carries a spiral phase profile corresponding to a specific topological charge and focal depth, enabling the formation of two spatially and spec-

trally separated vortex beams. The metalens leverages the frequency-dependent acoustic phase response to achieve this dual functionality within a single, compact lens. Building on the general principles introduced in Section 2.1, the focused acoustic vortex in each ring is realized by combining an azimuthally varying spiral phase with a concave acoustic lens profile. The azimuthal variation imparts the characteristic helical phase structure, while the concave profile ensures axial focusing of the beam. The phase delay introduced by the lens is governed by its local thickness. This thickness is directly related to the desired phase profile $\phi(r, \theta)$ as follows [22, 43, 44]:

$$
\phi(r,\theta)
\begin{cases}
\left[k_1 \left(\sqrt{r^2 + F_1{}^2} - F_1 \right) + l_1 \theta \right] \mathrm{mod} 2\pi, & 0 \leq r < r_{\mathrm{split}}, \\
\left[k_2 \left(\sqrt{r^2 + F_2{}^2} - F_2 \right) + l_2 \theta \right] \mathrm{mod} 2\pi, & r_{\mathrm{split}} \leq r \leq R,
\end{cases}
\tag{1}
$$

$$
h(r,\theta) = h_0 + \frac{\phi(r,\theta)}{k_{1,2} - k_{1,2\mathrm{lens}}},
\tag{2}
$$

where $h(r, \theta)$ is the thickness of the lens pixel positioned at a point with polar coordinates (r, θ), h_0 is the minimum thickness of the lens. $F_{1,2}$ represents focal depths for inner and outer zones of the lens with $k_{1,2}$ and $k_{1,2\mathrm{lens}}$ being the wave numbers in the medium and the lens material for the inner and outer lens rings, respectively. $l_{1,2}$ are the inner and outer vortex ring topological charges, respectively. These are integer-valued numbers that characterize the phase singularities of the acoustic field and quantify the number of 2π phase windings around each vortex core. They determine the orbital angular momentum carried by the acoustic wave and define the helical structure of its wavefront. R and r_{split} represent the total radius of the lens and the radius of the inner ring, respectively. Eqs. (1) and (2) enable the creation of the desired spiral focused phase profile for two different focal points, which varies from 0 to 2π, generating the required helical phase front combined with the focusing effect. As the spiral phase profile in each ring is fixed by design, the resulting vortex beams retain their assigned topological charge throughout strong interference. A frequency-domain simulation was conducted in COMSOL Multiphysics using a parametric sweep over the two design frequencies to extract the required thickness distribution for a full 2π phase shift and to confirm the results obtained analytically using the form $\Delta\phi = 2\pi f h (\frac{1}{c_{m1}} - \frac{1}{c_{m2}})$ with c_{m1} and c_{m2} are the speed of sound of medium one and two, respectively. This allowed precise tailoring of the metalens geometry to ensure high-efficiency vortex generation at both f_1 and f_2 respectively. A schematic illustration of the designed double-focused vortex beam can be seen in Fig. 1(a).

2.1.2 Tilted acoustic vortex beam generation

To generate an acoustic vortex beam with a tilted propagation axis, the phase profile of the metalens must be modified to introduce a lateral phase gradient. Unlike conventional vortex beams which are symmetrical and propagate along the surface normal, the phase gradient will induce a linear translation of the beam center as characterized by an angular deviation in its main propagation direction, while still preserving its orbital angular momentum characteristics. This functionality can be achieved by imposing a spatial phase gradient in the transverse plane, which imparts lateral momentum to the acoustic wave vector and steers the vortex beam in the desired direction without altering its helical phase structure. The final phase distribution $\phi(x,y)$ for the tilted vortex is given by [45, 46]

$$\phi(x,y) = \phi_{\text{vortex}}(x,y) + \phi_{\text{tilt}}(x,y), \tag{3}$$

where $\phi_{\text{vortex}}(x,y)$ represents the conventional spiral phase term used to generate the vortex, and $\phi_{\text{tilt}}(x,y)$ is the additional linear phase term. The tilt component can be expressed as

$$\phi_{\text{tilt}}(x,y) = k_x x + k_y y. \tag{4}$$

Here k_x and k_y are the spatial frequency components in the x and y directions, respectively, which control the magnitude and direction of the beam tilt. By adjusting these values, the vortex beam can be steered to propagate along a desired angle in space, as shown in Fig. 1(b). This combined phase distribution was encoded into the metalens geometry by mapping it to local variations in thickness, using the same phase-to-height conversion strategy described earlier.

2.1.3 Off-axis acoustic vortex beam generation

The generation of an off-axis acoustic vortex beam involves displacing the vortex core (phase singularity) from the center of the metalens, resulting in a beam whose phase singularity and pressure null are shifted laterally, while the beam itself still propagates along the surface normal. Unlike the tilted vortex beam, which redirects the entire beam, the off-axis configuration retains the axial propagation direction but alters the internal phase topology to create an asymmetrically structured vortex field. This is achieved by translating the center of the spiral phase profile to a new location (x_0, y_0) on the metalens. The resulting phase distribution becomes [47, 48]

$$\phi(x,y) = \text{mod}(\arctan(y - y_0, x - x_0), \, 2\pi). \tag{5}$$

Here, (x_0, y_0) denotes the new position of the phase singularity in the transverse plane. This displacement lifts the symmetry of the wavefront, causing the pressure null associated with the vortex core to shift away from

the beam axis. Despite this shift, the beam retains its helical phase and orbital angular momentum. The phase map generated using Eq. (5) is then translated into a spatial thickness profile across the metalens, using the same height-modulation technique employed in the previous designs, as can be seen illustrated in Fig. 1(c). A base height and maximum phase delay corresponding to 2π are maintained to ensure continuity with the fabrication.

2.2 Numerical simulation

This section presents the full-wave numerical simulations conducted in COMSOL Multiphysics to validate the functionalities outlined in Section 2.1. For the case of double-focused and off-axis vortex generation, simulations were performed using a unified model geometry: a spiral phase metalens with a total diameter of 30 mm, enclosed within a cylindrical fluid domain measuring 40 mm in diameter and 50 mm in height, concentric with the metalens. In the case of tilted acoustic vortex beam generation, a rectangular domain with a length of 50 mm, a width of 50 mm, and a height of 50 mm was employed. For all the cases, in order to emulate an open-water environment and suppress artificial reflections, impedance boundary conditions were applied to the lateral and top surfaces of the domain, and the surrounding medium was modeled as water. Furthermore, the metalens material properties were assigned based on cured SLA resin. Specifically, the density and speed of sound for the lens were set to $\rho_l = 1178$ kg/m³ and $c_l = 2591$ m/s, respectively, while the surrounding water was modeled with $\rho_m = 1000$ kg/m³ and $c_m = 1490$ m/s [49]. The simulations were carried out using the pressure acoustics, frequency domain interface, which solves the inhomogeneous Helmholtz equation to compute the acoustic pressure field and phase distribution. Under the assumption of lossless, adiabatic conditions, the governing equation takes the form [17]

$$\Delta \cdot \left(-\frac{1}{\rho}\Delta p_t\right) - \frac{k_{\text{eq}}^2 p_t}{\rho} = 0. \tag{6}$$

Here the material density is donated by ρ, the total pressure is presented by p_t, while k_{eq} represents the wave number that contains both the ordinary wave number $k = \frac{\omega}{c_l}$ as well as the out-of-plane wave number k_z, where ω is the angular frequency and c_l is the lens speed of sound. For excitation, a piezoelectric transducer source was modeled at the base of the lens and driven at a frequency of 1 MHz. To suppress non-physical reflections and emulate open-boundary conditions, impedance boundary conditions were applied along the lateral surface and top of the cylindrical and rectangular fluid domain. This setup ensures an accurate representation of the pressure field generated by the designed metalenses under realistic conditions.

085201-4

Chadi Ellouzi, et al., Front. Phys. 21(8), 085201 (2026)
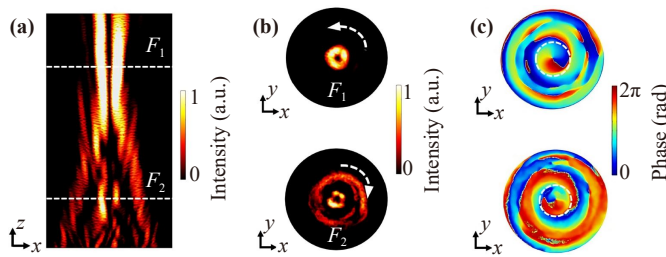
Fig. 2 Simulated pressure and phase distributions of the double-focused acoustic vortex beam generated by the frequency-multiplexed metalens operating at 1 MHz with different axial focal depths. **(a)** Simulated axial pressure field (xz plane) showing two distinct focal points F_1 and F_2 respectively. **(b)** Simulated transverse pressure distributions (xy plane) at the two focal depths: the upper panel corresponds to the focal point F_1, the lower panel corresponds to the focal point F_2. The white dotted arrow presents the rotation direction of the acoustic vortex. **(c)** Simulated transverse phase distributions (xy plane) at focal points F_1 (upper panel) and F_2 (lower panel), each exhibiting a clear 2π spiral phase pattern indicative of vortex behavior.

2.2.1 Double focused acoustic vortex beam generation

To evaluate the performance of the proposed metalens design for double-focused acoustic vortex generation, two simulation scenarios were conducted. Each scenario explores a distinct configuration of frequencies and focal lengths to assess the metalens's spatial and spectral multiplexing capabilities. In all simulations, the spiral phase metalens consisted of two concentric spiral phase regions, an inner ring and an outer ring, each independently encoding a helical phase profile corresponding to a specific topological charge and focal length. The pressure and phase fields were extracted to analyze the characteristics of the generated vortex beams. In the first configuration, both the inner and outer rings were driven at 1 MHz, with designed focal length $F_1 = 45$ mm for the outer ring and $F_2 = 20$ mm for the inner ring. The simulation results shown in Fig. 2 clearly reveal two distinct focal regions along the propagation axis corresponding to these target positions. Each vortex beam maintained a well-defined pressure null and exhibited a complete 2π spiral phase structure, confirming the preservation of its orbital angular momentum. This demonstrates that the metalens can spatially separate two vortex beams even when operating at the same frequency.

In the second and most representative scenario, the inner ring was driven at 600 kHz and the outer ring at 1 MHz, each designed with distinct focal lengths of $F_2 = 25$ mm and $F_1 = 35$ mm respectively. As shown in Fig. 3, this frequency-multiplexed configuration successfully generated two distinct focused vortex beams, both spatially and spectrally separated. Each beam retained a clear pressure null and phase spiral, with minimal cross-

interference. The use of separate excitation frequencies inherently reduces coupling between the concentric zones, as the 0.6 MHz and 1 MHz signals exhibit low spectral overlap. Combined with the differing focal depths, this frequency-based isolation enables independent vortex formation without requiring additional radial separation. These results demonstrate the metalens's ability to independently control multiple vortex beams within a single aperture by leveraging both geometric and frequency-domain multiplexing.

Collectively, the two simulation cases demonstrate the effectiveness and versatility of the proposed concentric-ring metalens design in producing multifunctional acoustic vortex beams. Each configuration showcases a different operating condition, ranging from spatial multiplexing at a single frequency to full spectral separation of independent vortex beams, thereby confirming the flexibility and adaptability of the metalens in practical scenarios.

2.2.2 Tilted acoustic vortex beam generation

To evaluate the performance of the metalens in steering acoustic vortex beams, numerical simulations were conducted for a set of configurations where a linear phase gradient was superimposed onto the spiral phase distribution. This approach enables angular control of the vortex beam without mechanical movement or additional elements. In this case, no focusing curvature was introduced, allowing the simulation to isolate and demonstrate the effect of phase-gradient-induced beam tilt. The metalens was excited at a frequency of 1 MHz, and a linear phase shift was applied in the x-direction to induce controlled steering at predefined tilt angles. Three scenarios were simulated: 0° (no tilt), 15°, and 25°, each corresponding to a different magnitude of the applied linear gradient. The resulting acoustic fields were analyzed to assess the effect of tilt on the vortex structure and beam trajectory.

Figure 4 presents a set of nine simulation results organized by tilt angles. Each row corresponds to one of the three tilt scenarios. The left column displays the axial pressure field, where the propagation direction and core displacement can be visualized. The middle column shows the top-view pressure field, highlighting the ring-shaped intensity profile associated with the vortex. The right column illustrates the phase distribution in the transverse plane, where the spiral structure indicates the presence and stability of the phase singularity. At 0° tilt, the vortex beam propagates symmetrically along the central axis. The axial pressure field displays a centered donut-shaped beam, and the phase pattern shows a clean, rotationally symmetric spiral centered on the origin. As the tilt angle increases to 15° and 25°, the vortex beam clearly deflects from the centerline. The axial pressure maps reveal a progressive lateral shift in the beam path, while the top-view pressure plots show
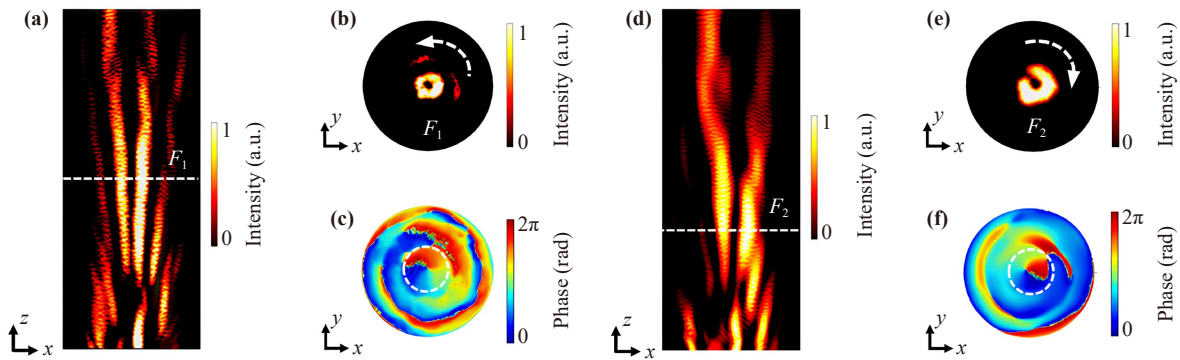
Fig. 3 Simulated pressure and phase distributions of the double-focused acoustic vortex beam generated by the frequency-multiplexed metalens operating at two distinct frequencies of 1 MHz (f_1) and 0.6 MHz (f_2) respectively, with different axial focal depths. **(a)** Axial pressure field (xz plane) at 1 MHz, showing the focal region corresponding to F_1. **(b)** Simulated transverse pressure distributions (xy plane) at the focal depth F_1. The white dotted arrow presents the rotation direction of the acoustic vortex. **(c)** Simulated transverse phase distributions (xy plane) at focal points F_1. **(d)** Axial pressure field (xz plane) at 0.6 MHz, showing the focal region corresponding to F_2. **(e)** Simulated transverse pressure distributions (xy plane) at the focal depth F_2. The white dotted arrow presents the rotation direction of the acoustic vortex. **(f)** Simulated transverse phase distributions (xy plane) at focal points F_2.

corresponding lateral shifts of the ring structure. Despite the change in propagation direction, the phase distribution in all cases retains its spiral form, indicating the vortex nature remains intact and the orbital angular momentum is preserved during propagation.

These results confirm that the metalens design effectively enables beam steering through passive phase control. The linear phase gradient successfully redirects the vortex beam while maintaining its core features and overall topological structure. The ability to adjust the

tilt angle without compromising beam integrity opens opportunities for non-mechanical beam scanning, directional particle manipulation, and adaptive acoustic routing in compact systems.

2.2.3 Off-axis acoustic vortex beam generation

To demonstrate the generation of an off-axis acoustic vortex beam, numerical simulations were conducted using a metalens with a displaced phase singularity.
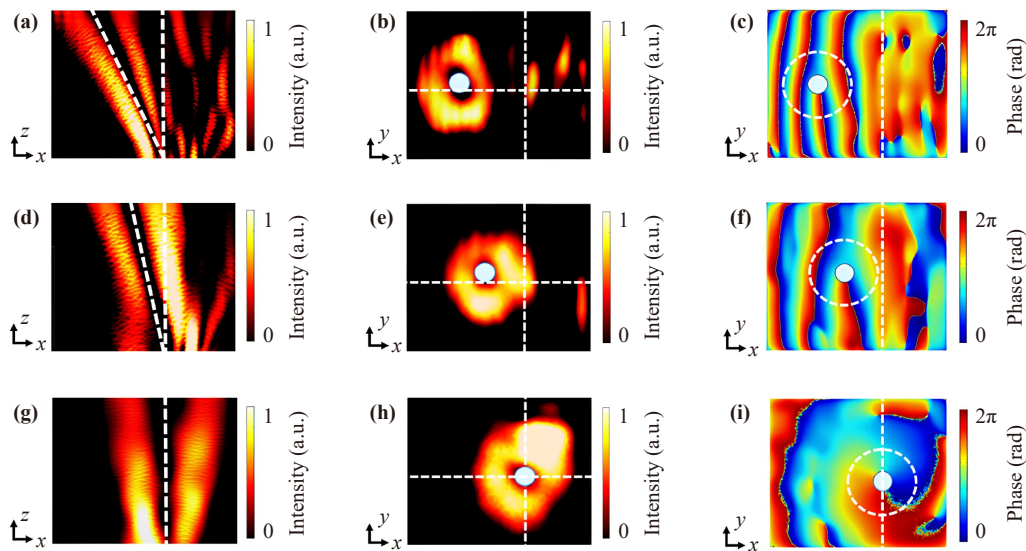
Fig. 4 Simulated results of tilted acoustic vortex beam generation for different tilt angles. Each row corresponds to a specific tilt of 25°, 15°, and 0°, respectively. **(a, d, g)** Axial pressure field showing beam trajectory and angular deviation. **(b, e, h)** Transverse pressure field illustrating lateral shift of the vortex ring. The cross of the white dotted lines marks the position of the vortex center without tilt. **(c, f, i)** Transverse phase distribution confirming preservation of vortex structure and topological charge.
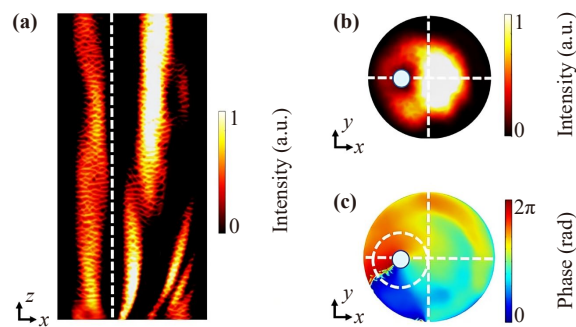
Fig. 5 Numerical simulation results for off-axis acoustic vortex beam generation. **(a)** Axial pressure distribution (xz plane) showing lateral displacement of the vortex beam. The white dotted line marks the position of the vortex center. **(b)** Transverse pressure field (xy plane) with off-centered vortex ring. **(c)** Transverse phase distribution (xy plane) illustrating the spiral structure centered around the displaced singularity. The cross of the white dotted lines marks the position of the domain center.

Instead of placing the vortex core at the geometric center of the aperture, the spiral phase distribution was shifted by introducing an offset in the coordinates of the phase function. This displacement effectively breaks the radial symmetry of the field and causes the vortex beam to emerge off the central axis of the propagation domain. The simulation was performed at a frequency of 1 MHz, with the phase profile defined to shift the singularity to a point (x_0, y_0) away from the center.

The simulation results for off-axis vortex generation are presented in Fig. 5. The axial pressure field in the xz plane, the top-view pressure distribution, as well as the transverse phase profile are depicted in Figs. 5(a)–(c), respectively. The results clearly show that the vortex beam propagates in a direction shifted from the central axis, with the pressure null displaced laterally. The top-view pressure ring is offset from the center, and the phase profile retains its spiral form but is centered around the displaced singularity. These results confirm that the position of the vortex core can be precisely controlled by adjusting the location of the phase singularity within the metalens aperture. The beam retains its vortex characteristics despite the shift, indicating that topological stability is preserved under spatial displacement. This capability is particularly useful for parallel beam generation, targeted acoustic delivery, and applications requiring localized vortex positioning without altering beam orientation or frequency.

3 Experimental results

To validate the acoustic performance of the metalens designs, three representative configurations were experimentally tested, namely a frequency-multiplexed metalens for generating dual acoustic vortex foci at distinct axial positions and frequencies (0.6 MHz and 1 MHz), a tilted vortex metalens designed to steer the vortex beam 15° along an off-normal propagation direction and an off-axis vortex beam generation. All prototypes were fabricated using a high-resolution stereolithography (SLA) 3D printer (Formlabs form 3) with a 25 μm layer resolution, well below the wavelength of the operating acoustic waves as shown in Figs. 6(b)–(d). This ensured precise reproduction of the designed thickness profiles and minimized surface-induced scattering. The metalenses were printed using standard clear resin, then post-cured for mechanical and acoustic stability. Each metalens had a diameter of 30 mm to match the aperture of the driving transducer. The metalens was mounted directly onto a circular piezoelectric ceramic transducer (SMR, Davenport, FL) with a 30 mm diameter and 2 mm thickness, resonant at 1 MHz. Excitation signals were generated using a function generator (RIGOL DG4162, Portland, OR), configured to emit Gaussian-shaped sinusoidal bursts with a 20% duty cycle. The signal was amplified using a broadband RF power amplifier (ENI 3200L, Renton, WA) to ensure sufficient acoustic intensity at the metalens interface. The generated acoustic fields were measured in a water tank using a needle hydrophone (NH0500, Precision Acoustics, Dorchester, UK) mounted on a 3D scanning stage. The scanning region covered an 80×80 grid in the transverse (xy) plane, capturing detailed spatial information of the pressure and phase distributions. At each scan point, the hydrophone recorded approximately 125 000 data samples using a digital oscilloscope, allowing high-fidelity reconstruction of the waveform. The schematic of the measurement setup is shown in Fig. 6(a).

To suppress spurious reflections and environmental noise, received signals were time-gated to temporally separate the primary transmitted wave from boundary reflections. The raw hydrophone signals were processed using a customized MATLAB script that applied a moving window function to isolate the main acoustic event and a 10 Hz high-pass Butterworth filter to eliminate low-frequency noise. Phase information was extracted by referencing the received signal to the input excitation, enabling accurate reconstruction of the vortex phase structures. Experimental results for all the configurations are summarized in Fig. 7, which presents the measured pressure amplitude and phase distributions.

For the dual-focus vortex lens, the measured pressure amplitude maps at each frequency clearly revealed two distinct focal spots located at different axial positions, confirming the metalens's ability to spatially separate the vortex beams. Each focal spot exhibited a pronounced donut-shaped pressure distribution with a near-zero pressure core, manifesting the unique characteristics of vortex beams with an orbital angular

Chadi Ellouzi, et al., Front. Phys. 21(8), 085201 (2026)

085201-7
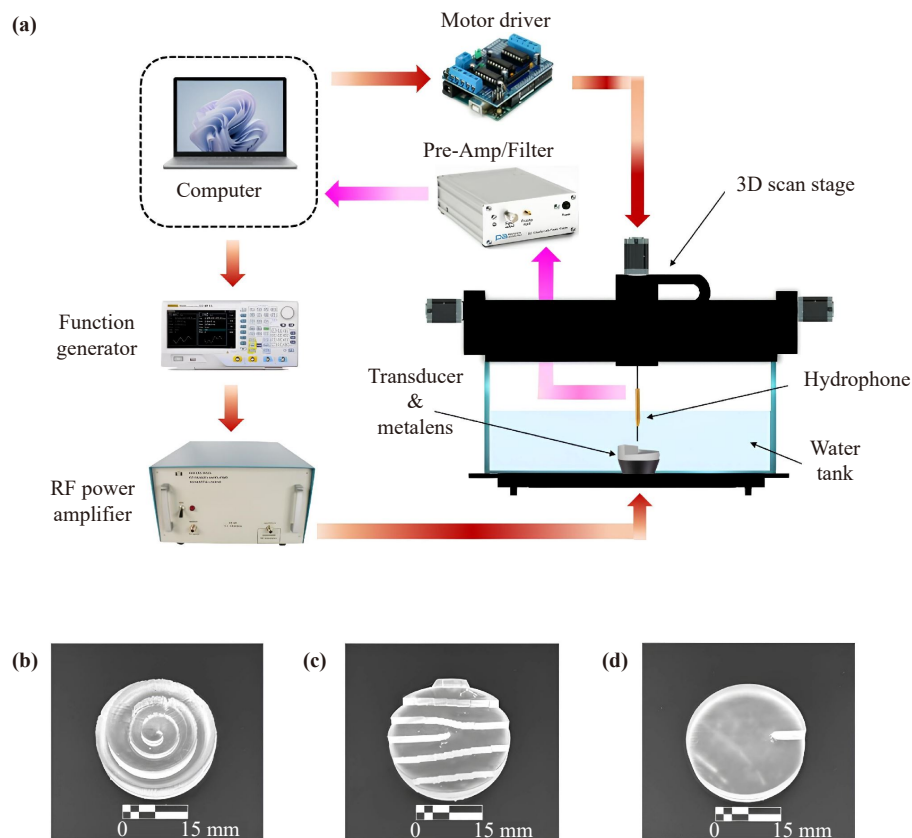
Fig. 6 Schematic of the measurement setup and the corresponding 3D printed metalenses. **(a)** Schematic of the experimental setup. **(b)** 3D printed metalens for double-focused acoustic vortex beam operating at two distinct frequencies of 1 MHz and 0.6 MHz, respectively, with different axial focal depths F_1 and F_2. **(c)** 3D printed metalens for a 15° tilted acoustic vortex beam generation. **(d)** 3D printed metalens for off-axis vortex beam generation.

momentum. Correspondingly, the phase maps demonstrated smooth, continuous 2π spiral phase variations around the vortex core, confirming the presence and stability of the topological singularities at both foci. Importantly, minimal interference and cross-talk was observed between the two focal regions, indicating effective frequency multiplexing and spectral selectivity of the metalens. In the tilted vortex beam experiments, the hydrophone scans showed a clear lateral shift of the acoustic vortex beam from the central axis, consistent with the intended phase gradient designed to steer the beam by 15°. The pressure amplitude profiles retained their characteristic ring-shaped vortex pattern, but these rings were displaced laterally in the direction of the applied phase gradient. Phase measurements further confirmed that the spiral phase structure and associated phase singularity remained intact despite the beam tilt, indicating preservation of the vortex's orbital angular momentum and topological charge. These results demonstrate the metalens's ability to steer vortex beams in a passive and non-mechanical manner, a feature critical for applications requiring flexible beam positioning without physical movement. For the off-axis vortex, the measurements clearly show that both the pressure and

phase centers are laterally shifted relative to the ideal centered position, consistent with the simulation results. To provide a quantitative assessment of the metalenses' performance and address the observed experimental deviations, additional measurements and analyses on the xz plane for both the dual-focus and tilted vortex configurations were conducted as can be seen in Fig. 8. The experimentally determined focal positions and tilt angles were extracted from both the transverse (xy) and axial (xz) pressure maps. The experimentally measured focal positions of the focused vortex were $F_{1ex} = 32.7$ mm (1 MHz) and $F_{2ex} = 24$ mm (600 kHz), corresponding to deviations of 6.6% and 4%, respectively from the theoretically designed focal points. For the tilted vortex metalens, designed for a 15° steering angle, the measured propagation tilt determined from the main-lobe displacement along propagation axis ($\Delta x/\Delta z$) yielded an experimental angle of ~14.2°, corresponding to a deviation of approximately 5.3%.

To further quantify the fidelity of the experimentally generated vortex phase structure, analysis was performed directly on the measured two-dimensional phase maps. A circular sampling path of diameter $D \approx \frac{D_{lens}}{2}$ was defined within each phase map and
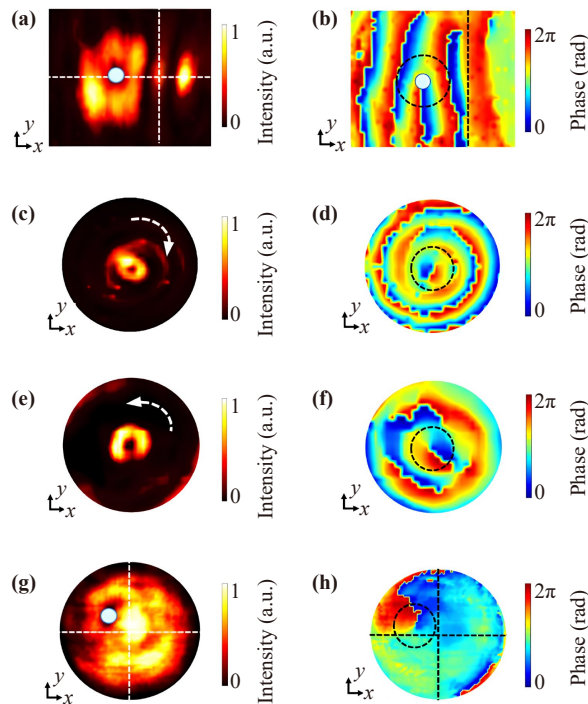
Fig. 7 Experimental results for a 15° tilted acoustic vortex beam, the double-focused acoustic vortex beam operating at two distinct frequencies of 1 MHz and 0.6 MHz, respectively, with different axial focal depths F_1 and F_2 and the off-axis vortex generation. **(a)** Transverse pressure distribution (xy plane) showing lateral displacement of the vortex beam. **(b)** Transverse phase distribution (xy plane) showing lateral displacement of the vortex beam. **(c)** Transverse pressure field (xy plane) at 1 MHz, showing the focal region corresponding to F_1. The white dotted arrow presents the rotation direction of the acoustic vortex. **(d)** Transverse phase distributions (xy plane) at the focal point F_1. **(e)** Transverse pressure distributions (xy plane) at 0.6 MHz, showing the focal region corresponding to the focal depth F_2. The white dotted arrow presents the rotation direction of the acoustic vortex. **(f)** Transverse phase distributions (xy plane) at focal points F_2. **(g)** Transverse pressure field (xy plane) of off-axis acoustic vortex at 1 MHz. The cross of the white dotted lines marks the position of the domain center. **(h)** Transverse phase distributions (xy plane) of the off-axis vortex. The black dotted circle marks the location of the vortex center.

centered at the phase singularity corresponding to the vortex core. The phase values along this path were extracted, yielding a one-dimensional representation of the phase evolution as a function of the azimuthal coordinate. The extracted experimental phase profile was then compared to the ideal phase expected for a vortex of topological charge $l = 1$, which exhibits a continuous phase increase from 0 to 2π over one full revolution. The phase deviation between the experimental and ideal profiles was computed and wrapped within the interval $[-\pi, \pi]$. The root-mean-square (RMS) value of this wrapped phase deviation quantifies the average departure
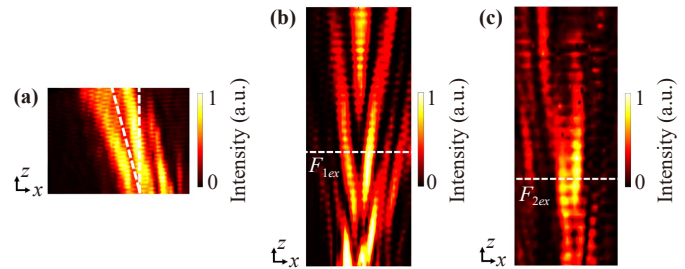
Fig. 8 Experimental results in the xz plane for a 15° tilted acoustic vortex beam and the double-focused acoustic vortex beam operating at two distinct frequencies of 1 MHz and 0.6 MHz, respectively, with different axial focal depths F_{1ex} and F_{2ex}. **(a)** Axial pressure distribution showing lateral displacement of the vortex beam. **(b)** Axial pressure field (xz plane) at 1MHz, showing the focal region corresponding to F_{1ex}. **(c)** Axial pressure distributions (xz plane) at 0.6 MHz, showing the focal region corresponding to the focal depth F_{2ex}.

of the measured phase from the ideal helical structure. Based on this metric, the phase fidelity (P) was defined as [11, 50]

$$P = 1 - \left(\frac{RMS(\Delta\phi)}{2\pi l} \right), \tag{7}$$

where $\Delta\phi$ represents the wrapped phase deviation from the ideal helical phase. The measured phase fidelity values were $P_1 = 0.91$ (1 MHz focus), $P_2 = 0.89$ (0.6 MHz focus), $P_{TB} = 0.88$ (tilted beam), and $P_{OA} = 0.92$ (off-axis beam), respectively, indicating high phase fidelity across all cases. It is worth noting that the imposed azimuthal phase during the design of the vortex lens guarantees that the generated underwater acoustic field carries a vortex with topological charge l. However, the detailed mode coefficients of the generated vortex depend on the amplitude distribution, which can vary with the structural modulation, acoustic loading of water, and finite-aperture effects. These variations modify the radial-mode composition but do not affect the global phase circulation or the robustness of the vortex charge, which is the quantity relevant for our analysis. Nonetheless, some inconsistencies were observed when comparing numerical simulations to experimental outcomes. Specifically, the overall phase fields produced were not ideal, exhibited minor deviations in smoothness and clarity compared to simulations. In experiments with the double-focused acoustic vortex lens, there was a minor misalignment of the produced vortex beam from the center of the metalens. In the case of the tilted vortex beam, more prominent refractions were observed in the experimental results. Furthermore, for the off-axis vortex, the characteristic doughnut-shaped pressure ring was less well-defined and exhibited distortions compared to the ideal simulated pattern, indicating slight diffraction and irregularities in the

beam profile. These deviations between simulations and measurements may stem from the inaccuracies in the phase profile resulting from manufacturing errors, surface roughness, and impurities affecting the sound speed in water. Other factors for the inconsistency can also be attributed to the fluctuation generated by the transducer throughout the experimental procedures. Nevertheless, the aforementioned experimental errors could be reduced by improving the efficiency of the transducer and reducing the step size during data collection.

Overall, the experimental data aligns well with numerical simulations, validating the metalens designs and their various capabilities in real-world underwater environments. The clear formation of dual focal vortex beams at distinct frequencies, the precise angular steering of vortex beams and the off-axis vortex generation underscore the practical potential of these 3D-printed metalenses for advanced acoustic manipulation in various scenarios.

4   Conclusion

This study presents a generalized design and fabrication framework for the generation and control of underwater acoustic vortex beams using 3D-printed spiral phase metalenses. Numerical simulations and experimental validations confirm the successful implementation of advanced beam-shaping functionalities, including dual-focus vortex beam generation with frequency multiplexing, precise control of beam tilt, and off-axis vortex displacement. The proposed framework enables multiple function-specific metalenses, each derived from the same phase-engineering methodology, to achieve tunable spatial and spectral control of acoustic fields. The use of high-resolution 3D printing facilitates accurate reproduction of complex phase profiles with subwavelength precision, enabling effective operation in underwater environments without reliance on large transducer arrays. The demonstrated frequency multiplexing and passive beam steering capabilities highlight the versatility and scalability of the approach for future adaptive acoustic systems. By unifying diverse functionalities within a single design strategy, this work establishes a practical pathway toward advanced acoustic manipulation, targeted ultrasound therapy, and multi-channel underwater communication.

References

1. J. L. Thomas and R. Marchiano, Pseudo angular momentum and topological charge conservation for nonlinear acoustical vortices, *Phys. Rev. Lett.* 91(24), 244302 (2003)

2. J. Zhang, K. Yang, H. Luo, P. Li, F. Wen, Y. Gu, and Z. Wu, Modulation of orbital angular momentum of vortex beam based on ordered pinhole screens, *Results Phys.* 51, 106713 (2023)

3. I. Martynyuk-Lototska, M. Kostyrko, D. Adamenko, I. Skab, and R. Vlokh, Generation of acoustic vortices and acousto-optic interactions with acoustic vortex beams, *Appl. Opt.* 62(14), 3643 (2023)

4. C. Liu, Y. Ye, and J. H. Wu, Tunable broadband acoustic vortex generator with multiple orders based on mie resonances structure, *Adv. Mater. Technol.* 8(13), 2202082 (2023)

5. X. D. Fan, Z. Zou, and L. Zhang, Acoustic vortices in inhomogeneous media, *Phys. Rev. Res.* 1(3), 032014 (2019)

6. Y. Fu, C. Shen, X. Zhu, J. Li, Y. Liu, S. A. Cummer, and Y. Xu, Sound vortex diffraction via topological charge in phase gradient metagratings, *Sci. Adv.* 6(40), eaba9876 (2020)

7. C. Zhou, Q. Wang, S. Pu, Y. Li, G. Guo, H. Chu, Q. Ma, J. Tu, and D. Zhang, Focused acoustic vortex generated by a circular array of planar sector transducers using an acoustic lens, and its application in object manipulation, *J. Appl. Phys.* 128(8), 084901 (2020)

8. M. Cromb, G. M. Gibson, E. Toninelli, M. J. Padgett, E. M. Wright, and D. Faccio, Amplification of waves from a rotating body, *Nat. Phys.* 16(10), 1069 (2020)

9. C. Shi, M. Dubois, Y. Wang, and X. Zhang, High-speed acoustic communication by multiplexing orbital angular momentum, *Proc. Natl. Acad. Sci. USA* 114(28), 7250 (2017)

10. S. Zhao, N. Zhang, P. Han, Y. Gu, and H. Dong, Enhanced broadband manipulation of acoustic vortex beams using 3-bit coding metasurfaces through topological optimization, *Small* 20(19), 2308349 (2024)

11. R. Li, C. Liu, L. Wang, C. Ma, J. Wu, and F. Ma, Tunable acoustic vortex generation by a compact rotating disk, *Commun. Phys.* 7(1), 188 (2024)

12. R. Amiri, M. Mahdavi, and M. Mahmoudi, Acoustic-vortex generation through orbital angular momentum transfer, *Phys. Rev. A* 109(2), 023523 (2024)

13. W. Wang, C. Hu, J. Ni, Y. Ding, J. Weng, B. Liang, C. Qiu, and J. Cheng, Efficient and high-purity sound frequency conversion with a passive linear metasurface, *Adv. Sci. (Weinh.)* 9(33), 2203482 (2022)

14. C. Liu, H. Long, C. Ma, Y. Jia, C. Shao, Y. Cheng, and X. Liu, Broadband acoustic vortex beam generator based on coupled resonances, *Appl. Phys. Lett.* 118(14), 143503 (2021)

15. M. Baudoin, J. L. Thomas, R. Al Sahely, J. C. Gerbedoen, Z. Gong, A. Sivery, O. B. Matar, N. Smagin, P. Favreau, and A. Vlandas, Spatially selective manipulation of cells with single-beam acoustical tweezers, *Nat. Commun.* 11(1), 4244 (2020)

16. H. Tang, Z. Chen, N. Tang, S. Li, Y. Shen, Y. Peng, X. Zhu, and J. Zang, Hollow-out patterning ultrathin acoustic metasurfaces for multifunctionalities using soft fiber/rigid bead networks, *Adv. Funct. Mater.* 28(36), 1801127 (2018)

17. C. Ellouzi, A. Zabihi, F. Aghdasi, A. Kayes, M. Rivera, J. Zhong, A. Miri, and C. Shen, Underwater double vortex generation using 3D printed acoustic lens and field multiplexing, *APL Mater.* 12(3), 031130 (2024)

18. J. Jang and J. Chang, Design and fabrication of double-focused ultrasound transducers to achieve tight focusing, *Sensors (Basel)* 16(8), 1248 (2016)

19. Z. Li, G. Hu, Q. Wang, and L. Du, Research on a focused acoustic vortex that can be used to capture tiny underwater objects, *Water* 16(20), 2954 (2024)

20. P. Wu, Z. Ya, Y. Li, M. Zhu, L. Zhang, Y. Zong, S. Guo, and M. Wan, Focused acoustic vortex-regulated composite nanodroplets combined with checkpoint blockade for high-performance tumor synergistic therapy, *ACS Appl. Mater. Interfaces* 14(27), 30466 (2022)

21. C. Liu, X. Hu, Z. Li, X. Cao, and X. Fu, A strategy for fast and precise control of polarity and chirality in magnetic vortices, *Front. Phys. (Beijing)* 20(2), 22201 (2025)

22. J. Li, A. Crivoi, X. Peng, L. Shen, Y. Pu, Z. Fan, and S. A. Cummer, Three dimensional acoustic tweezers with vortex streaming, *Commun. Phys.* 4(1), 113 (2021)

23. S. Jiménez-Gambín, N. Jiménez, and F. Camarena, Transcranial focusing of ultrasonic vortices by acoustic holograms, *Phys. Rev. Appl.* 14(5), 054070 (2020)

24. J. Zhao, X. Wei, C. Fei, Y. Li, Z. Li, L. Lou, Y. Quan, and Y. Yang, Phase-optimized multi-step phase acoustic metasurfaces for arbitrary multifocal beamforming, *Micromachines (Basel)* 14(6), 1176 (2023)

25. T. Li, J. Li, L. Bo, H. Bachman, B. Fan, J. Cheng, and Z. Tian, Robot-assisted chirality-tunable acoustic vortex tweezers for contactless, multifunctional, 4-DOF object manipulation, *Sci. Adv.* 10(21), eadm7698 (2024)

26. X. D. Fan, Z. Zou, and L. Zhang, Acoustic vortices in inhomogeneous media, *Phys. Rev. Res.* 1(3), 032014 (2019)

27. X. D. Fan and L. Zhang, Acoustic orbital angular momentum Hall effect and realization using a metasurface, *Phys. Rev. Res.* 3(1), 013251 (2021)

28. N. Ding, T. Feng, Q. Wang, Z. Chen, G. Guo, Y. Li, J. Tu, D. Zhang, and Q. Ma, Multitarget manipulation of off-axis acoustic vortices based on a focused sector-vortex transducer array, *Phys. Rev. Appl.* 22(5), 054012 (2024)

29. W. Li, S. J. Dai, Q. Y. Ma, G. P. Guo, and H. P. Ding, Multiple off-axis acoustic vortices generated by dual coaxial vortex beams, *Chin. Phys. B* 27(2), 024301 (2018)

30. Y. Li, W. Li, Q. Ma, G. Guo, J. Tu, and D. Zhang, Regulation of multiple off-axis acoustic vortices with a centered quasi-plane wave, *J. Appl. Phys.* 124(11), 114901 (2018)

31. Q. Wang, C. Liu, C. Song, H. Ding, X. Wang, and Y. Li, Chirality-protected extreme asymmetric acoustic information transport with noise immunity, *Nat. Commun.* 16(1), 8066 (2025)

32. Q. Wang, Z. Zhou, D. Liu, H. Ding, M. Gu, and Y. Li, Acoustic topological beam nonreciprocity via the rotational Doppler effect, *Sci. Adv.* 8(40), eabq4451 (2022)

33. M. E. Kelly and C. Shi, Design and simulation of acoustic vortex wave arrays for long-range underwater communication, *JASA Express Lett.* 3(7), 076001 (2023)

34. J. F. Pazos-Ospina, F. Quiceno, J. L. Ealo, H. R. D. Muelas, and J. Camacho, Focalization of acoustic vortices using phased array systems, *Phys. Procedia* 70, 183 (2015)

35. J. F. Pazos-Ospina, J. L. Ealo, and E. E. Franco, Characterization of phased array-steered acoustic vortex beams, *J. Acoust. Soc. Am.* 142(1), 61 (2017)

36. Y. Li, X. Jiang, B. Liang, J. Cheng, and L. Zhang, Metascreen-based acoustic passive phased array, *Phys. Rev. Appl.* 4(2), 024003 (2015)

37. X. Jiang, Y. Li, and L. Zhang, Thermoviscous effects on sound transmission through a metasurface of hybrid resonances, *J. Acoust. Soc. Am.* 141(4), EL363 (2017)

38. Z. Hao, H. Chen, Y. Yin, C. W. Qiu, S. Zhu, and H. Chen, Efficient conversion of acoustic vortex using extremely anisotropic metasurface, *Front. Phys. (Beijing)* 19(4), 42202 (2024)

39. H. W. Dong, C. Shen, Z. Liu, S. D. Zhao, Z. Ren, C. X. Liu, X. He, S. A. Cummer, Y. S. Wang, D. Fang, and L. Cheng, Inverse design of phononic meta-structured materials, *Mater. Today* 80, 824 (2024)

40. S. Pu, G. Guo, X. Guo, C. Zhou, Y. Li, Q. Ma, J. Tu, and D. Zhang, Auto-focusing acoustic-vortex tweezers for obstacle-circumventing manipulation, *J. Appl. Phys.* 130(23), 234903 (2021)

41. S. Guo, Z. Ya, P. Wu, and M. Wan, A review on acoustic vortices: Generation, characterization, applications and perspectives, *J. Appl. Phys.* 132(21), 210701 (2022)

42. R. Marchiano, F. Coulouvrat, L. Ganjehi, and J. L. Thomas, Numerical investigation of the properties of nonlinear acoustical vortices through weakly heterogeneous media, *Phys. Rev. E* 77(1), 016605 (2008)

43. T. Kusaka, and T. Tanaka, Fast and accurate approximation methods for trigonometric and arctangent calculations for low-performance computers, *Electronics (Basel)* 11(15), 2285 (2022)

44. E. Agiasofitou and M. Lazar, Mathematical modeling of electro-elastic dislocations in piezoelectric materials, *Proc. Appl. Math. Mech.* 22(1), e202200167 (2023)

45. A. Biswas, C. L. Zekios, and S. V. Georgakopoulos, An ultra-fast method for designing holographic phase shifting surfaces, *Sci. Rep.* 13(1), 16511 (2023)

46. S. Zheng, Z. Zhao, and W. Zhang, Versatile generation and manipulation of phase-structured light beams using on-chip subwavelength holographic surface gratings, *Nanophotonics* 12(1), 55 (2023)

Chadi Ellouzi, et al., Front. Phys. 21(8), 085201 (2026)

085201-11

47. I. Augustyniak, W. Lamperska, J. Masajada, Ł. Płociniczak, and A. Popiołek-Masajada, Off-axis vortex beam propagation through classical optical system in terms of kummer confluent hypergeometric function, *Photonics* 7(3), 60 (2020)

48. M. Guo, W. Le, C. Wang, G. Rui, Z. Zhu, J. He, and B. Gu, Generation, topological charge, and orbital angular momentum of off-axis double vortex beams, *Photonics* 10(4), 368 (2023)

49. M. Bakaric, P. Miloro, A. Javaherian, B. T. Cox, B. E. Treeby, and M. D. Brown, Measurement of the ultrasound attenuation and dispersion in 3D-printed photopolymer materials from 1 to 3.5 MHz, *J. Acoust. Soc. Am.* 150(4), 2798 (2021)

50. Y. Shen, X. Wang, Z. Xie, C. Min, X. Fu, Q. Liu, M. Gong, and X. Yuan, Optical vortices 30 years on: OAM manipulation from topological charge to multiple singularities, *Light Sci. Appl.* 8(1), 90 (2019)

085201-12

Chadi Ellouzi, et al., Front. Phys. 21(8), 085201 (2026)